Diffusive boundary layers over varying topography

R. W. Dell[1,†] and L. J. Pratt[2]

[1]Climate, Atmospheric Science, and Physical Oceanography, Scripps Institution of Oceanography,
UC – San Diego, San Diego, CA 92093, USA

[2]Department of Physical Oceanography, Woods Hole Oceanographic Institution,
Woods Hole, MA 02543, USA

Diffusive bottom boundary layers can produce upslope flows in a stratified fluid. Accumulating observations suggest that these boundary layers may drive upwelling and mixing in mid-ocean ridge flank canyons. However, most studies of diffusive bottom boundary layers to date have concentrated on constant bottom slopes. We present a study of how diffusive boundary layers interact with various idealized topography, such as changes in bottom slope, slopes with corrugations and isolated sills. We use linear theory and numerical simulations in the regional ocean modeling system (ROMS) model to show changes in bottom slope can cause convergences and divergences within the boundary layer, in turn causing fluid exchanges that reach far into the overlying fluid and alter stratification far from the bottom. We also identify several different regimes of boundary-layer behaviour for topography with oceanographically relevant size and shape, including reversing flows and overflows, and we develop a simple theory that predicts the regime boundaries, including what topographies will generate overflows. As observations also suggest there may be overflows in deep canyons where the flow passes over isolated bumps and sills, this parameter range may be particularly significant for understanding the role of boundary layers in the deep ocean.

Key words: boundary-layer structure, geophysical and geological flows, ocean processes

1. Introduction

In the deep ocean, mixing and upwelling are needed to balance deep water formation, maintain the stratification and dissipate the kinetic energy input by winds and tides. In physical terms, mixing transports mass upward and converts kinetic to potential energy, while upwelling is vertical volume transport. Though the physical oceanography community has long had estimates of the total integrated amounts of mixing and upwelling (for example Munk 1966), we do not adequately understand their distribution in space and time. Modelling studies show that different distributions of mixing can lead to very different ocean circulations. For example, Huang & Jin (2002) found in models of the Atlantic that the same total mixing produces different

† Email address for correspondence: dell@ucsd.edu

deep circulations if the mixing distribution is changed. To model and predict ocean circulation, we need the distribution of diffusivity, and for that we need to understand the mechanisms of mixing and upwelling.

Currently, the physical oceanography community devotes most attention to mechanisms concerned with mixing from internal wave breaking. However, diffusive boundary layers on sloping bottoms are a potentially significant source of both mixing and upwelling. This was recognized when they were first described by Phillips (1970) and Wunsch (1970). Subsequent work has further elucidated the behaviour of these boundary layers with rotation (Thorpe 1987), when the viscosity and diffusivity vary with distance from the bottom (Garrett 1991), the time-adjustment of the boundary layers (MacCready & Rhines 1991), and the response of the boundary layers to periodic forcing in time (Umlauf & Burchard 2011). Laboratory experiments by Peacock, Stocker & Aristoff (2004) have confirmed the analytical solution of Phillips and Wunsch, and explored boundary layers with sharp stratification gradients that force exchanges with the far field (Phillips, Shyu & Salmun 1986; Salmun & Phillips 1992). These laboratory studies prefigure some of the key results of this paper, describing how gradients in stratification and turbulent diffusivity can force exchanges between the boundary layer and the far field. However, all of these studies have concentrated on boundary layers over constant-slope bottom boundaries. A rare study that includes the effect of a change in bottom slope is Page & Johnson (2009), who studied the boundary-layer response in a diamond-shaped box with heated walls: a very interesting study, but not concerned with oceanographic applications.

Unfortunately, the ocean bottom is anything but a smooth constant slope. In fact, there is growing observational evidence that diffusive boundary layers may arise precisely in the complicated topography of the mid-ocean ridge flank canyons. Thurnherr and coauthors see the characteristic bottom-intensified upslope flow and isopycnals bending down to intersect the bottom in multiple such canyons, and also measure strongly increased turbulence in the same places (for example Thurnherr *et al.* 2005 and St. Laurent & Thurnherr 2007). The turbulence in these canyons is so strong that Thurnherr *et al.* (2005) estimate that as much as half of all of the mixing in the deep Brazil Basin may be happening in ridge-flank canyons, though they occupy only 10 %–15 % of the basin area.

Inspired by these observations, this study begins to examine how diffusive boundary layers behave over complex topography. We begin by reviewing the known boundary-layer solution for an infinite constant slope, and discussing the characteristics of that solution that will be important when the bottom slope varies (§ 2). Then, after reviewing the numerical methods (§ 3), we present a series of numerical experiments involving increasingly complicated types of idealized topography. The first numerical experiments examine a single change in bottom slope (§ 4), then move on to corrugations on a background slope (§ 5) and sills (§ 6). In all of these cases, we focus primarily on oceanographically relevant values for bottom slope, stratification and size of topography. This paper deals only with non-rotating boundary layers. The effects of rotation in both two-dimensional and three-dimensional domains are the subject of forthcoming work.

The major themes that emerge are that changes in bottom slope drive exchange of large volumes of fluid between the boundary layer and the far field, connecting the dynamics and stratification of the two regions; and that interactions with topography do not only modulate the bottom boundary-layer flow, but can actually change its geometry.
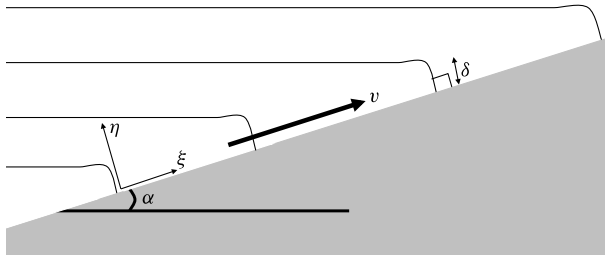
FIGURE 1. Schematic of diffusion-driven boundary-layer flow. The thin black lines are surfaces of constant density. To satisfy the no-flux boundary condition, they must bend down to intersect the bottom at a right angle. This creates a horizontal pressure gradient, driving an upslope velocity (v). The key variables illustrated here are: α, the slope angle; $\delta = 1/\gamma$, the boundary-layer thickness scale; and (ξ, η) the along-slope and slope-normal coordinates.

2. Constant-slope solution and expected response to varying slope

Phillips (1970) and Wunsch (1970) both presented an analytical solution for diffusive boundary layers over a constant bottom slope α. The concept behind this type of boundary layer is simple and elegant. If there is no flux of density from the boundary, the slope-normal density gradient must go to zero at the boundary. If the bottom boundary is sloping, this no-flux boundary condition causes isopycnals to bend downward to intersect the slope at a right angle, as shown schematically in figure 1. This in turn creates a horizontal pressure force because denser fluid is at the same depth as lighter, and this drives an upslope flow. Both authors assumed Boussinesq dynamics over an infinite constant slope, and found a boundary layer with a bottom-intensified upslope jet:

$$v(\eta) = 2\kappa\gamma \cot\alpha\, \mathrm{e}^{-\gamma\eta} \sin\gamma\eta \qquad (2.1)$$

where v is the upslope velocity, η is the slope-normal coordinate and α is the constant slope angle, as shown in figure 1. The thickness scale of the boundary layer, δ, is given by

$$\delta = \frac{1}{\gamma} = \left(\frac{4\nu\kappa}{N^2 \sin^2\alpha}\right)^{1/4}. \qquad (2.2)$$

Higher rates of mixing ν (viscosity) and κ (diffusivity) are associated with thicker boundary layers, as is stronger stratification (smaller N). Smaller bottom angle α is also associated with a thicker boundary layer. A typical theoretical velocity profile with its bottom-intensified upslope current is shown in figure 2(a), compared with a numerically calculated velocity field.

There are two aspects of this solution that suggest variations in bottom slope α might have dramatic effects on the boundary layer. First, we can derive the horizontal length scale over which the boundary layer responds to changes. This spatial scale L arises from the adjustment timescale τ, the time required for diffusion to act across the thickness of the boundary layer δ:

$$\tau \sim \frac{\delta^2}{\kappa} \sim \frac{\sqrt{Pr}}{N \sin\alpha}. \qquad (2.3)$$
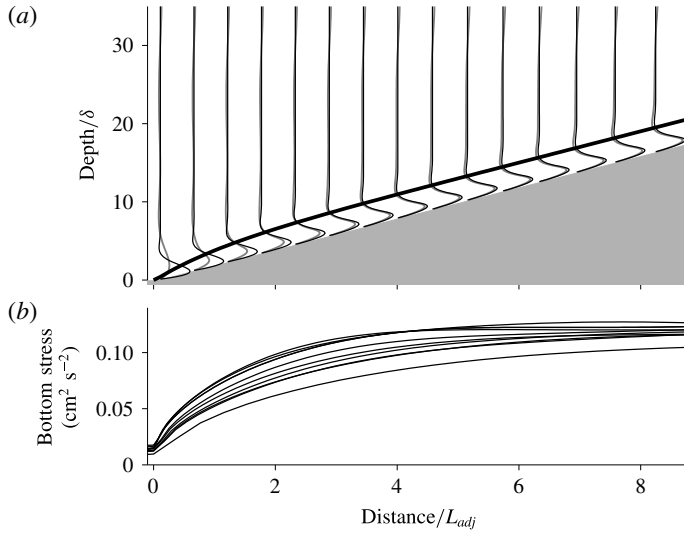
FIGURE 2. The boundary layer requires a length scale L to accelerate to its constant-slope solution. The upper plot (*a*) compares the constant-slope solution from (2.1) (thin black lines) to numerically calculated velocity profiles at various points along a slope. The area where the *x*-axis is less than 0 has a flat bottom, and the diffusion-driven boundary layer starts at 0. The thick black line shows the predicted thickening of the boundary layer as it accelerates over the distance L. The bottom slope in this simulation is $\alpha_0 = 0.022$. The lower plot (*b*) shows the bottom stress as a function of along-slope position for 10 simulations with bottom slopes ranging from $0.01 < \alpha < 0.12$, again with along-slope distance normalized by L.

Here Pr is the Prandtl number, ν/κ. To get the spatial scale, we multiply τ by the boundary-layer velocity scale from (2.1):

$$L \sim \upsilon\tau \sim 2\delta \cot\alpha \sim \frac{(\kappa\nu)^{1/4}}{N^{1/2}} \frac{\cos\alpha}{\sin^{3/2}\alpha}. \qquad (2.4)$$

Overall, $L \sim \alpha^{-3/2}$ for small angles, so steeper slopes with thinner boundary layers adjust over shorter distances. Before doing any detailed calculations or numerical simulations, we can see that if the bottom slope changes on scales much larger than L, the constant-slope solution should be approximately correct everywhere. However, if the bottom slope changes on scales smaller than L, the boundary layer might behave very differently. This adjustment scale also helps to resolve an apparent contradiction in the Phillips/Wunsch solution, namely that the boundary-layer thickness and velocity appear to go to infinity as the bottom slope angle goes to zero. As $\alpha \to 0$ the time τ and space L required to adjust to that solution go to infinity even faster, so it takes an infinitely long time and infinitely much space for the boundary layer to adjust to the steady-state solution where υ is unbounded. No real finite physical system would ever get there.

The second reason that we expect changes in the bottom slope to have dramatic effects on the boundary layer comes from the total volume flux in the boundary layer. Phillips noted that integrating the density equation from the boundary to limit where

$\eta \to \infty$ yielded a remarkably compact expression for the total boundary-layer flux Q:

$$Q = \int_0^\infty v \, \mathrm{d}\eta = -\frac{g}{\rho_0 N^2 \sin \alpha} \left. (\kappa \nabla \rho) \right|_0^\infty = \kappa \cot \alpha. \qquad (2.5)$$

The total boundary flux Q is given by the diffusivity κ and the bottom slope α. Therefore, if the slope changes, we expect that fluid will be either forced out of the boundary layer or entrained into it, coupling the dynamics of the boundary layer to the far field.

There is a good physical reason why the boundary-layer flux Q is set by the diffusivity and bottom slope. In a diffusive stratified fluid, there is a continuous background flux of density up (or buoyancy down, if you prefer) in the far field. However, approaching the bottom boundary, which we assume has no density flux across it, there will inevitably be a flux divergence. The upslope, and so upward, advective mass flux in the boundary layer replaces the mass being mixed up by diffusion in the interior, compensating for that flux divergence. More diffusive flux (larger κ) requires a stronger boundary-layer flux Q to compensate for it. A steep bottom slope (larger α) means the boundary-layer flux has a larger vertical component and can more easily compensate for a vertical diffusive flux divergence, so a steeper slope implies a smaller total boundary-layer flux Q.

In the subsequent sections, we will see the effects of both the adjustment length of the boundary layer and the slope dependence of the boundary-layer flux in numerical simulations of diffusive boundary layers over varying bottom topography. Before that, however, we describe the technical details of the numerical simulations that follow.

3. Numerical methods and validation of scaling

We performed a series of two-dimensional, non-rotating numerical experiments using the regional ocean modeling system (ROMS), developed by Shchepetkin & McWilliams (2005). ROMS is a fully nonlinear hydrostatic primitive equation model. It has a free surface and topography-following coordinates, also known as σ-coordinates.

We present numerical experiments on a range of idealized topography, including constant bottom slopes, localized changes in slopes, sinusoidal corrugations on slopes and isolated sills. Mixing in the model was represented as an explicitly specified eddy diffusivity κ and eddy viscosity ν with eddy Prandtl number $Pr = \nu/\kappa = 1$. For most simulations, we took $\nu, \kappa = 5 \times 10^{-3}$ m^2 s^{-1}, the mean value Thurnherr *et al.* (2005) inferred from turbulent microstructure measurements in abyssal canyons. All results use these values unless otherwise specified. For completeness, we replicated simulations with ν, κ one-half this value and one-tenth this value; the dynamics in these simulations were consistent with the simulations with larger ν, κ. Given the eddy viscosity, the Reynolds number Re was small in all of the numerical experiments. The no-slip bottom boundary condition was approximated using a strongly enhanced linear bottom drag. The results were insensitive to the specific value of the coefficient of drag. No surface stress was applied. Unless otherwise specified, the stratification was $N^2 = 10^{-5}$ s^{-2}, also taken from the observations of Mid-Atlantic Ridge canyons of Thurnherr *et al.* (2005).

The numerical experiments were initialized with zero velocity throughout the domain and the velocity field was allowed to come to a steady state. The time to steady state is the boundary-layer time scale τ, defined in (2.3). It was typically several hours, and the simulations were run for 2–3 days to ensure it was truly

steady. By the end of the simulations, the acceleration term in the momentum budget was no more than 1 % the value of the leading-order dynamical balance. For each type of numerical experiment, we tested numerical convergence by duplicating key experiments with doubled horizontal and/or vertical resolution. We took results to have converged only if the differing resolutions agreed to within 3 %. The final experiments have vertical grid spacing that varied from about 0.5 m in the bottom boundary layer to about 15 m in the far field. For comparison, the boundary-layer thickness $\pi\delta$ in our parameter range was 20–125 m.

Simulations with zero mean bottom slope used closed lateral boundaries. In simulations with a mean bottom slope, we used open boundary conditions because the background stratification made periodic boundaries impossible. The open boundary conditions specified that the barotropic flux through the domain was $Q = \kappa \cot \alpha$, calculated in (2.5). They also specified the full, depth-dependent, baroclinic momentum at the outflowing boundary. In order to match the flow to this outflowing boundary condition, a long uninterrupted section of constant slope topography was inserted between the study region and the boundaries. This section was typically 2–10 times the length scale for boundary-layer adjustment, L, given in (2.4). To ensure the free surface had no effect, the domain was always at least 35δ deep. As with convergence in resolution, we performed tests for each type of topography to ensure the boundary conditions were not affecting the boundary-layer behaviour. We doubled the domain size, and if the resulting velocity field changed by less than 3 %, considered the domain sufficiently large. For clarity, the figures in this paper show only the study region, not the full domain.

The best test of the accuracy of this numerical approach is the theoretical solution for a constant slope given in (2.1). The adjustment to this constant-slope solution is shown in figure 2. The computational domain has a large area on the left with a flat bottom and no diffusion-driven boundary-layer flow and an area of constant slope on the right. The thin black profiles in figure 2(*a*) show the constant-slope solution, while the grey lines show the numerically calculated velocity after it has reached a steady state in time. The numerically calculated boundary layer flow accelerates along the slope, and approaches the constant-slope profile over the distance scale L, given in (2.4). By several distances of L along the slope, the velocity field matches the Phillips/Wunsch solution to within 4 %. Multiple such boundary-layer adjustment simulations with bottom slopes ranging from $\alpha = 0.01$ to $\alpha = 0.12$ confirm that the velocity field adjusts over length scale L given in (figure 2*b*). For this range of slopes, L varies by a factor of 40, but the velocity field and bottom stress in all cases asymptotically approaches its constant value within a few L.

4. Changes in slope and exchange with far field

Even the simplest possible varying topography, the bottom slope changing at a single location, creates interesting dynamics. Any change in the slope will change the boundary layer flux Q, given in (2.5), and so entrain fluid into the boundary layer or force fluid out of it in an intrusion (figure 3). This allows the boundary layer to affect the flow and stratification far from the bottom. We can derive the density of the fluid in the intrusion with a mass budget and demonstrate that fluid is exchanged between the boundary layer and the far field at its level of neutral buoyancy. An appropriate control volume for the mass budget is bounded upstream and downstream of the change in slope far enough away that the boundary layer velocity was not affected by the change in slope and bounded above far enough from the bottom that the intrusion cannot reach the top.
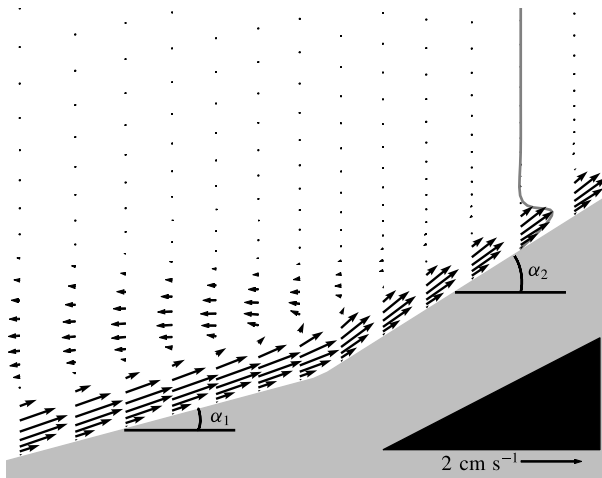
FIGURE 3. A single change in the bottom slope forces fluid out of the boundary layer and into the far field. Away from the change in slope, the boundary-layer velocity returns to the constant slope solution (2.1), shown in the grey velocity profile near the right-hand side of the figure. The numerically simulated boundary-layer velocity shown in the arrows matches the theoretical prediction to within 4 %. $\alpha_1 = 0.026$ and $\alpha_2 = 0.061$. As in all figures, the black triangle is 1 km wide and 50 m tall.

The mass flux M_{int} of the intrusion into the far field is the residual of the mass flux in the boundary layer over slope α_1, the mass flux in the boundary layer over slope α_2, and the vertical diffusive mass flux in the background stratification. The volume flux in the intrusion Q_{int} is just the difference of Q_1 and Q_2, the volume fluxes in the boundary layers over the two slopes (from (2.5)). This gives the average density of the fluid exchanged between the boundary layer and the far field:

$$\rho_{int} = \frac{M_{int}}{Q_{int}} = \rho_0 \left(1 - \frac{5}{4} \frac{N^2}{g} \frac{Q_1 \delta_1 \cos \alpha_1 + Q_2 \delta_2 \cos \alpha_2}{Q_1 + Q_2} \right) \qquad (4.1)$$

where ρ_0, the background density, is set to be the bottom density at the change in slope. In 22 numerical experiments with slopes ranging from $0.01 < \alpha < 0.11$, the predicted density of the intrusion agreed with the numerical results to within 3 %. In comparison to the intrusion density, the far-field fluid at the depth spanned by the thickness of the boundary layer has density in the range ρ_0 to $\rho_0 (1 - ((N^2 \pi \delta)/(g \cos \alpha)))$. A little bit of straightforward algebra shows that ρ_{int} always falls in this range: fluid enters and leaves the boundary layer at its level of neutral buoyancy, so the boundary layer is not expected to generate vertical velocities or static instability in the far field. However, as we see in the next section, the exchange of water between the boundary layer and the far field still alters the background stratification.

5. Boundary-layer flow geometry over corrugated slopes

Just as a single change in bottom slope can cause a point exchange between the boundary layer and the far field, a continuously varying bottom can cause exchanges continuously throughout the water column. In this section, we look at

bottom topography with well-defined horizontal length scales and see the effect of the space L required for the boundary layer to adjust to its constant-slope solution. This section considers topography made of a constant background slope with sinusoidal corrugations superimposed:

$$h(y) = \alpha_0 y + A \sin \frac{2\pi y}{\lambda} \tag{5.1}$$

where h is the topography, y is the horizontal distance, α_0 is the background slope, A is the half-height of the corrugations and λ is the length of the corrugations. We can describe the topography completely in terms of three non-dimensional parameters:

$$\frac{\delta_0}{A} = X_1 = \frac{\text{Boundary layer thickness}}{\text{Corrugation height}} \tag{5.2}$$

$$\frac{\alpha_0}{2\pi A/\lambda} = \frac{\Delta h}{A} = X_2 = \frac{\text{Background slope}}{\text{Slope of corrugation}} \tag{5.3}$$

$$\frac{A}{\lambda} = X_3 = \frac{\text{Corrugation height}}{\text{Corrugation length}} \tag{5.4}$$

where δ_0 is the boundary-layer thickness associated with the background slope α_0, calculated using (2.2) and $\Delta h = \alpha \lambda / 2\pi$ is the vertical separation between two adjacent corrugations. As these parameter values change, so does the behaviour of the bottom boundary layer. Since we are primarily interested in the oceanographic relevance of these boundary layers, we will restrict our study to topography that is much longer than it is tall; $X_3 < 0.02$ in all cases presented.

All corrugations have areas of increasing slope and decreasing slope, leading to both intrusions and entrainment. The simplest case is small-amplitude corrugations, where the corrugations are not tall enough to reverse the bottom slope anywhere ($\Delta h / A > 1$). As long as the boundary layer is no thicker than A, this implies that $L < \lambda$ and the boundary layer can be approximated with the locally constant-slope assumption. We call this the linear geometry. Since the boundary-layer flux Q changes along-slope, the corrugations cause a stack of alternating exchange flows between the boundary layer and the far field (figure 4a, showing an example where $\alpha_0 = 0.02$, $A = 10$ m and $\lambda = 6000$ m). The volume fluxes of these exchanges can be similar to or more than the volume flux in the boundary layer itself. This selectively adds fluid of a given density to or removes it from the far field, sharpening or weakening far-field stratification at the level of changes in topographic slope (figure 5). This effect penetrates into the far field and spreads vertically (in z) according to the scale derived in Koh (1966):

$$z^3 \sim y \frac{\sqrt{\nu \kappa}}{N}. \tag{5.5}$$

Eventually the outflowing current spreads vertically enough to overlap with the inflowing currents above and below, until the currents cancel one another out. This sets the scale of the maximum penetration of the stratification effect of the boundary on the far field. That slope-normal thickness scales like

$$D \sim \lambda^3 \left(\frac{N}{\sqrt{\nu \kappa}} \right) \sin^4 \alpha_0. \tag{5.6}$$
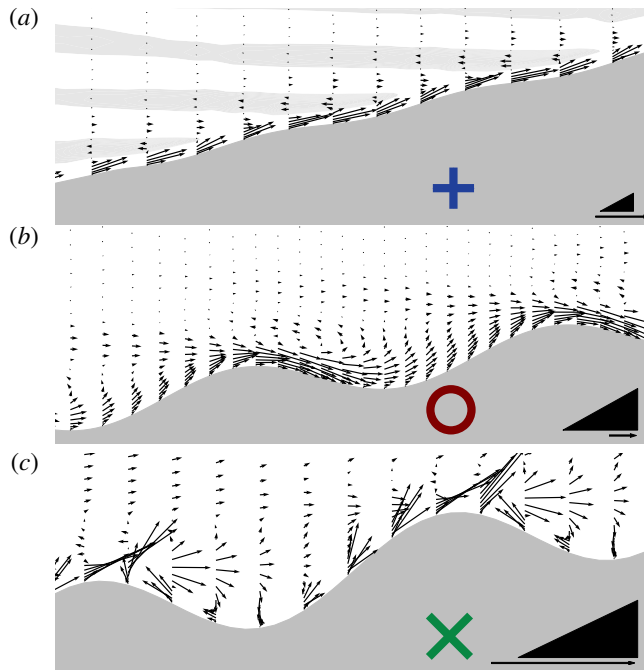
FIGURE 4. (Colour online) Example velocity fields induced by boundary-layer dynamics over a corrugated sloping bottom. Depending on the size and shape of the topography, there are three principle boundary-layer geometries: (*a*) linear, (*b*) overflow and (*c*) reversing. In (*a*), the intrusion layers are shown with light grey shading where the horizontal velocity is leftward, away from the bottom boundary layer. In each plot, the black triangle is 1 km wide and 50 m tall, and the small arrow beneath the triangle shows 2 cm s^{-1}. The large markers ($+$, $\bigcirc$, $\times$) are a legend to identify the boundary-layer geometries in the regime diagram presented later in the paper (figure 11). The parameter values for each simulation are given in the text.

At small slopes, this distance depends very sensitively on the mean slope α_0 and the corrugation wavelength λ. In real oceanic topography, these values vary constantly, so any estimate of D has significant uncertainty. In our numerical models, D ranges from more than 20 km to over 1000 km, vastly greater than the size of our numerical domain or the depth of the ocean. We therefore cannot verify D directly, but we feel it is a physically relevant length scale that deserves further consideration. It suggests that the full depth of the ocean may feel the effects of the boundary-layer dynamics.

If we move from small-amplitude topography to the other extreme, very large-amplitude corrugations ($\Delta h/A \ll 1$, $\delta_0/A \ll 1$), the geometry of the boundary-layer flow changes considerably, but many aspects of the dynamics remain similar. The boundary-layer flow is upslope on both faces of each corrugation, both upstream and downstream of the sill (figure 4*c*, showing an example where $\alpha_0 = 0.02$, $A = 35$ m, $\lambda = 3000$ m and ν, $\kappa = 5 \times 10^{-4}$ m^2 s^{-1}). Right at the sill, the horizontal velocity goes to zero and the boundary-layer flux leaves the boundary layer vertically. We call this behaviour reversing, since the boundary-layer velocity changes sign. Here, too, the locally constant-slope assumption provides a reasonable estimate of the boundary-layer behaviour, as here, too, $L \ll \lambda$.
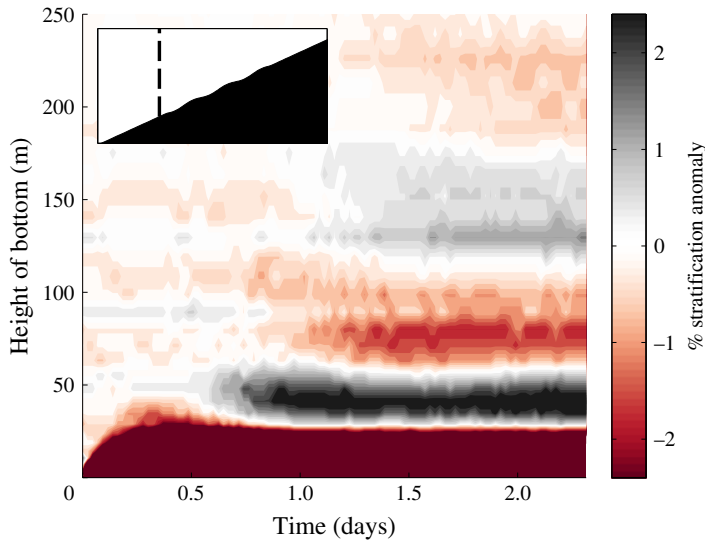
FIGURE 5. (Colour online) Density anomalies far from the bottom are created by boundary-layer dynamics over a slope with small-amplitude corrugations. This is a depth–time diagram of the evolution of the stratification anomaly in the column indicated with a dashed line in the inset. Stratification is strengthened at some depths, weakened at others, as fluid is drawn into or forced out of the boundary layer. Results are from the same small-corrugation-amplitude numerical experiment whose velocity field is shown in figure 4(*a*).

As is often the case in fluid mechanics, however, the most interesting things happen not at either extreme, but when everything is order one. When the slope of the corrugations is similar to the background slope ($\Delta h/A \sim 1$) and the amplitude of the topography is similar to the thickness of the boundary layer ($\delta_0/A \sim 1$), the boundary layer's behaviour changes dramatically. The boundary layer accelerates at the sill and forms an overflow into the trough behind it (figure 4*b*, showing an example where $\alpha_0 = 0.012$, $A = 25$ m and $\lambda = 4200$ m). The locally constant-slope assumption breaks down completely. Downstream of the sill, it would give not just the wrong answer, but the wrong sign of the answer. In fact, in these overflow cases, the largest velocities are found immediately downstream of the sill, exactly where the locally constant-slope assumption would predict flow in the opposite direction. The velocities are large enough that the Richardson number *Ri* falls below 0.25, the threshold for shear instability, for most of the thickness of the boundary layer. We call this geometry overflow.

The momentum balance confirms that locally constant-slope approximation is appropriate for very small and very large topography, but quite wrong for topography in the middle. For very small and very large topography, with linear and reversing boundary layers, the dominant momentum balance is the same as for a constant slope: between pressure generated by the no-flux bottom boundary condition and vertical viscosity (figure 6*a*,*b*). Advection is negligible (figure 6*c*). For an overflow (figure 6*d*–*f*), the advection is of the same order as the boundary-condition-driven pressure gradient and the viscous dissipation in the neighbourhood of the sill.

In summary, corrugations produce three distinct types of flow behaviour in the boundary layer, with each type of behaviour corresponding to a distinct parameter
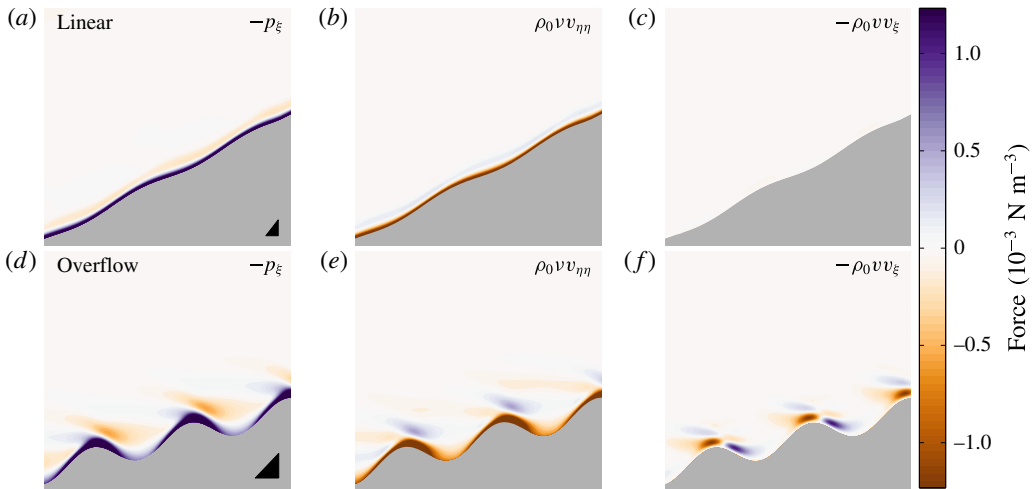
FIGURE 6. Leading order momentum balance for boundary layers with linear and overflow geometries. For small-amplitude topography (*a*–*c*), the dynamics remain substantively linear, with the pressure gradient (*a*) balancing the viscous dissipation (*b*) and negligible advection (*c*). This is the same momentum balance as in the constant-slope case. For topography with plunging overflows (*d*–*f*) like that shown in figure 4(*b*), the dynamical balance requires significant advection (*f*). The parameter values for these simulations can be found in the captions to figure 4. As in all figures, the black triangle is 1 km wide and 50 m tall.

range: linear, overflow and reversing. Only the overflows have significant advection. We would like to be able to predict quantitatively how a boundary layer will behave over a given topography. In the next section, we will further idealize the topography to develop that prediction, and find that bottom stress is the salient quantity.

6. Understanding overflows

In the previous section, we saw that the boundary layer at a sill could behave in different ways, leading to different flow geometries over a corrugated slope. To develop a quantitative prediction of the behaviour of the boundary layer, it is useful to look at an even simpler model topography: a single isolated sill. We will see in this section that the bottom stress at the sill controls which sills develop overflows and which do not, then apply that to understanding the results of the previous section.

6.1. *Asymmetrical sills and the role of bottom stress*

The question of when an overflow will form is highlighted in figure 7. Three sills, each with left slope $\alpha_1 = 0.065$ and right slope $\alpha_2 = -0.105$, have three different outcomes. One has an upslope flow on both sides of the sill, with the two boundary-layer fluxes exiting the boundary layer vertically at the top of the sill (figure 7*a*,*b*); one has an overflow from the shallow-slope side of the sill to the steeper side (figure 7*c*,*d*); and one has an overflow from the steep-slope side to the shallow slope (figure 7*e*,*f*). The only difference among the three cases is that the slopes have been lengthened or shortened.

The adjustment behaviour of a boundary layer over a single constant slope helps explain these various behaviours. On either side of the sill, the bottom boundary layer
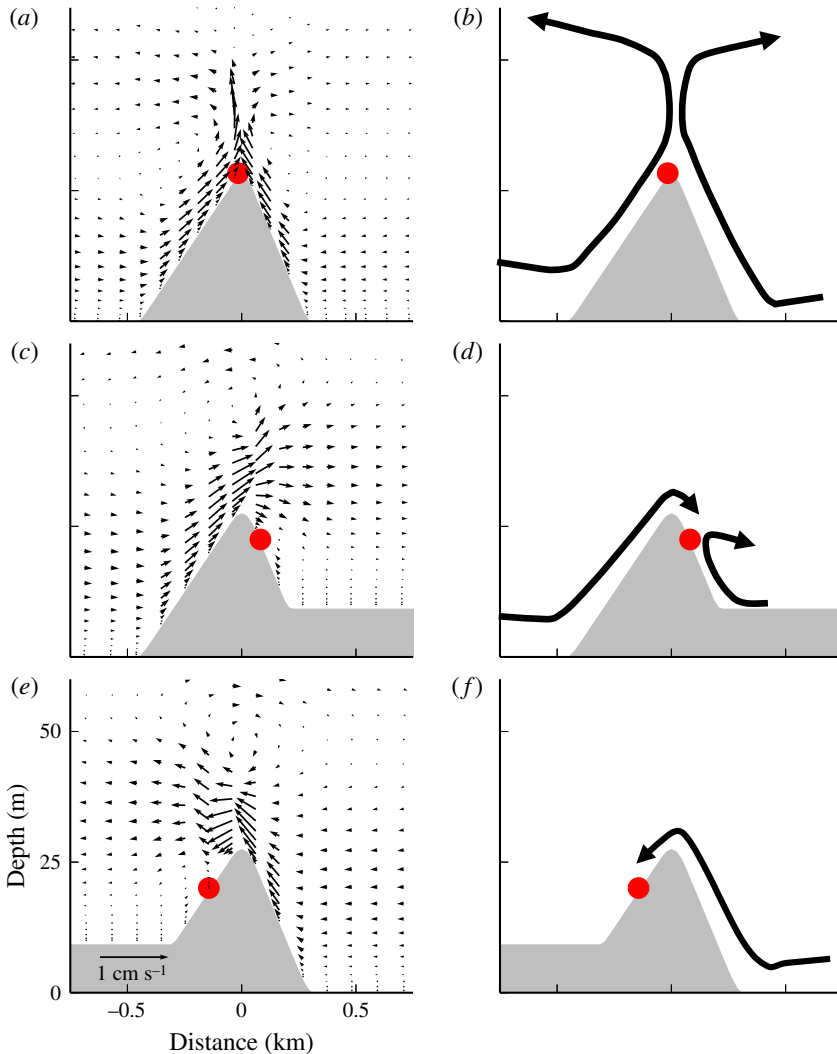
FIGURE 7. (Colour online) Asymmetrical sills with the same side slopes can develop an overflow at the sill in either direction. Three sills with the same slopes, shown with a velocity field on the left and a schematic based on streamlines on the right, can have either no overflow (*a*,*b*), an overflow from shallow slope to steep (*c*,*d*) or from steep slope to shallow (*e*,*f*). The strength and direction of the overflow can be characterized by the distance from the sill to the point of boundary-layer separation, indicated with a large dot. In all cases the left slope is $\alpha_1 = 0.065$ and right slope is $\alpha_2 = -0.105$, with the vertical distance from the flat bottom to the top of the sill either 20 or 30 m.

is adjusting to its constant-slope solution. At the bottom of the slope the adjustments on either side happen independently of each other. Using single-slope simulations for the respective slopes, like that used to validate the adjustment length scaling L (figure 2), we can see what the boundary layer on each side of the sill would be doing at the sill if the boundary layer on the other side did not exist. A schematic of this approach, treating each side of the sill as the beginning of a constant slope,
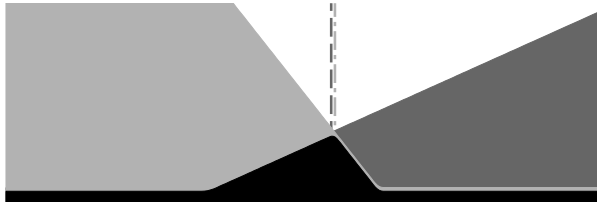
FIGURE 8. Schematic of estimation of bottom stress at a sill. To understand how the boundary layer will behave at a sill (black topography), we look at simulations of the boundary layer adjusting to the constant slope of each face of the sill. We compare profiles (dashed lines) taken over constant slopes (light and dark grey topography) at the same distance from the flat bottom as the sill top. An example of the profiles associated with each side are shown in figure 9.
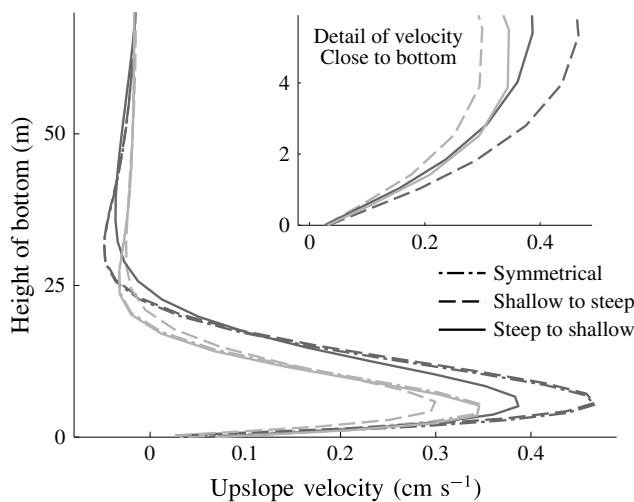

FIGURE 9. The boundary-layer velocities associated with each side of a sill show that the shallower slope has a faster current almost everywhere in the water column. These profiles are calculated as diagrammed in figure 8, with the darker profiles showing the shallower slope boundary layer and paler profiles the steeper slope. The dot-dashed profiles show the two boundary layers associated with the sill in figure 7(*a,b*), the dashed show the sill in figure 7(*c,d*), and the solid profiles correspond to figure 7(*e,f*). The inset plot is a detail of the 5 m closest to the bottom. The velocity from the steeper side expected to be greater only close to the bottom in the steep to shallow overflow case. Therefore, this is the only case where the expected bottom stress at the sill is greater on the steep side.

is shown in figure 8. For both the shallow and steep sides of the sill, we take a velocity profile from the constant-slope boundary-layer adjustment simulations at the location where the sill would be. Regardless of the different overflow behaviours, in all cases and almost everywhere in the water column the velocities associated with the shallower slope are faster than those from the steeper slope (figure 9). The shallow-slope boundary layer is both thicker and faster, as its infinite-constant-slope solution would suggest.

If we look very close to the bottom, though, the shallow-slope boundary layer is not always faster. Where there is a shallow-to-steep overflow, the near-bottom velocity

and so the bottom stress is larger on the shallow side. Where there is a steep-to-shallow overflow, the near-bottom velocity and bottom stress are larger on the steep side (figure 9, inset), even though the velocity is greater on the shallow side almost everywhere in the water column. The sign of the bottom stress s controls the direction of the overflow. A laminar boundary layer separates from the bottom where flow is converging and the bottom stress goes to zero (Prandtl, 1904, cited in Weldon *et al.* (2008)). This point of zero bottom stress, also known as the stagnation point, is directly tied to the direction and strength of an overflow, because the boundary layer separates at the maximum extent of the overflow. For stronger overflows, the stagnation point is farther down the opposite slope. The stagnation point for each case is marked with a large circle in figure 7; it is taken to be where s is zero.

By combining the constant-slope solution and the adjustment scale L, we can estimate the bottom stress s at the sill without having to do a full numerical simulation. As we saw in figure 2(*b*), the bottom stress s approaches a constant value over the length scale L, approximately like

$$s(\xi) = \nu \frac{\partial u}{\partial \eta}\bigg|_{\eta=0} = s_0 \left(1 - e^{-\xi/L}\right) \tag{6.1}$$

s_0 is the constant bottom stress of the infinite-constant-slope bottom boundary layer, calculated from (2.1):

$$s_0 = \nu \frac{\partial u}{\partial \eta}\bigg|_{\eta=0} = 2\frac{\kappa \nu}{\delta_0^2}\cot \alpha_0 = \sqrt{\kappa \nu} N \cos \alpha_0. \tag{6.2}$$

We combine the estimated bottom stress from either side of a sill to estimate it at the sill itself:

$$\text{Estimated bottom stress} = s_e = s_1(\xi_{sill}) - s_2(\xi_{sill}) \tag{6.3}$$

where s_1 and s_2 are the bottom stresses of the slopes of each face of the sill. Putting these three equations together, our estimated bottom stress at the sill s_e depends only on the two slopes α_1 and α_2 and the lengths of the two sides, ξ_1 and ξ_2:

$$s_e = N \cos \alpha_0 \sqrt{\kappa \nu}\left(\exp\left(-\frac{\xi_2}{2\delta_2 \cot \alpha_2}\right) - \exp\left(-\frac{\xi_1}{2\delta_1 \cot \alpha_1}\right)\right) \tag{6.4}$$

δ_1, δ_2 are known functions of α_1, α_2, given in (2.2). If the bottom stress at the sill is greater than zero, we expect an overflow from left to right; if it is less than zero, we expect an overflow from right to left; and if it is about zero, we expect no overflow.

This relationship between bottom stress and overflows is confirmed by numerical simulations of isolated sills. The location of the stagnation point calculated with a full numerical simulation is strongly correlated with the bottom stress at the sill estimated from only the shape of the topography (figure 10). Strong overflows are associated with estimated bottom stresses in the direction of the overflow, while runs without an overflow have little or no estimated bottom stress. A linear least-squares fit shows that bottom stress estimated from nothing but the shape of the topography captures 71 % of the variance in both the direction and the strength of overflows at the sills. Though the best fit line does not pass through the point (0, 0), it is less than one standard deviation away.

This result is useful in two ways. First, it confirms that bottom stress controls whether an overflow forms and how strong it is. Second, we can apply this understanding to more complicated topography such as corrugations on a slope to predict under what circumstances an overflow will form.
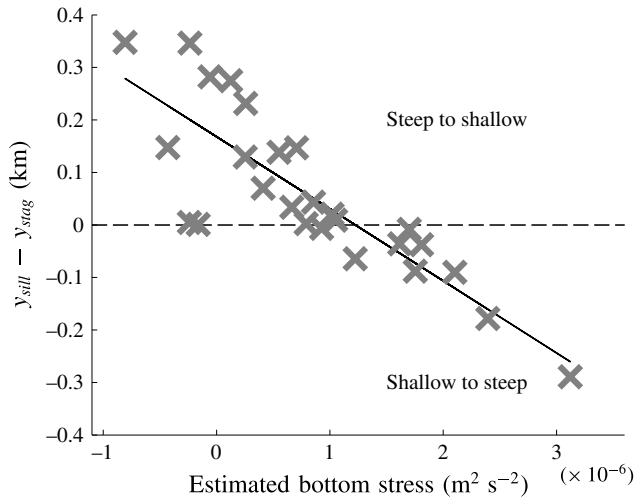
FIGURE 10. The virtual bottom stress, composed from simulations on constant slopes, is strongly correlated with the strength of an overflow in a simulation of an asymmetrical sill. The strength of the overflow is indicated by the location of the stagnation point in the boundary layer over an asymmetrical sill (y_{stag}) relative to the location of the top of the sill (y_{sill}). The location of the stagnation point and the estimated bottom stress come from different sets of numerical experiments and are calculated independently. A total of 71 % of the variance in more than 30 simulations is explained by a simple linear fit (black line).

6.2. *Predicting flow over corrugations with bottom stress*

We can apply the prediction from § 6.1 of the strength and direction of sill overflows to the corrugated slope numerical experiments in § 5. This will give another test of the salience of bottom stress in determining boundary-layer behaviour.

Corrugated slopes showed three bottom boundary-layer geometries: linear, that were well-described by making a locally constant-slope assumption; overflows, where the boundary layer accelerated at the sill and flows down into the trough behind it; and reversing, with upslope flows on both faces of each corrugation. An example of each is shown in figure 4. To predict whether an overflow will form, we estimate the bottom stress s as in the previous section. The peak of each corrugation can be approximated as an isolated sill; with the horizontal peak-to-trough distance giving ξ_1, ξ_2, the slope lengths. For a corrugated slope, the estimated bottom stress s_e at the sill from (6.4) is

$$s_e = s_0 \left[\exp \left(-\frac{\cos^{-1} X_2}{2X_1}(1 - X_2)\sqrt{\frac{X_2 - 1}{X_2}} \right) \right.$$
$$\left. - \exp \left(-\frac{2\pi - \cos^{-1} X_2}{2X_1}(1 + X_2)\sqrt{\frac{X_2 + 1}{X_2}} \right) \right]. \quad (6.5)$$

This expression assumes that the bottom slope is small everywhere. Under this assumption, the estimated bottom stress at the sill does not depend on the third non-dimensional parameter describing the topography, $X_3 = A/\lambda$. If $s_e > 0$, the stagnation point is downstream of the sill and we expect an overflow; if it is not, we do not.
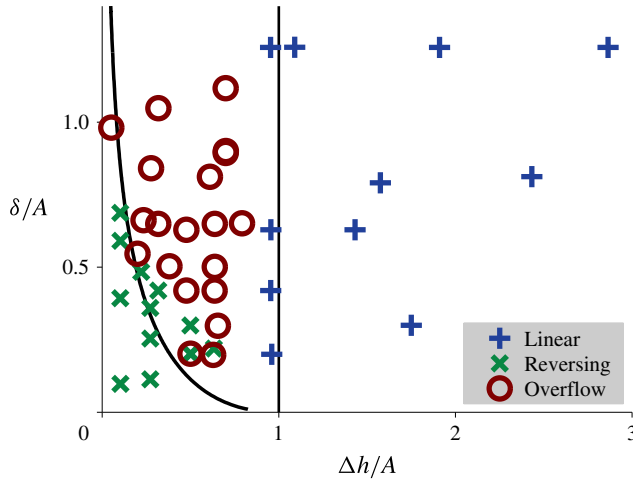
FIGURE 11. (Colour online) The behaviour of the boundary layers over corrugated slopes are separated in non-dimensional parameter space. The x-axis is a ratio of the background slope to the slope of the corrugations, and the y-axis is the ratio of the boundary-layer thickness to the height of the corrugations. The symbols refer to the flow geometry, summarized in figure 4: linear ($+$), overflow ($\bigcirc$) and reversing ($\times$). The predicted boundaries between the different geometries are shown as black contours: the curved line showing where bottom stress goes to zero at the peak of the sill and the straight line showing where the bottom stress becomes positive everywhere. These predictions are based entirely on the topography, and require no direct numerical computation.

The predictions can be compared with the numerical results in the (X_1, X_2) plane (figure 11). The three types of flow are well separated in this parameter space. As expected, the linear boundary layers ($+$) are all found in or near the region where bottom stress is positive everywhere in the domain ($X_2 = \Delta h/A > 1$). The contour defining topographies where the stagnation point from (6.5) is expected to be exactly at the peak of the sill approximately separates the overflows ($\bigcirc$) from the reversing boundary layers ($\times$). We do not expect the prediction to be perfect because it is based on a sill where two constant slopes meet at a point, not a continuously varying sinusoidal corrugation and there is a weak effect from variation in X_3. Broadly, however, the numerically simulated corrugations behave as predicted.

7. Discussion and conclusions

We have explored the effects of a varying slope α on the behaviour of flow in a diffusive and viscous boundary layer, especially its effect on the overlying stratified fluid. Because the volume flux Q varies with α, spatial changes in α are expected to result in convergences and divergences within the boundary layer. A numerical model confirms this, showing that mass is drawn into the boundary layer from the overlying fluid when the slope is decreasing and forced out of the boundary layer into the overlying fluid when the slope is increasing. In the case of a single transition from a shallow constant slope to the steep constant slope, the expelled fluid forms a horizontal intrusion that penetrates far into the ambient fluid (e.g. figure 3). The average density and volume flux in the intrusion predicted by mass balance (4.1) agree quite well with the model.

A sloping bottom with periodic corrugations can produce a series of alternating inflows and outflows that affect fluid far from the bottom. In our numerical model, the alternating inflows and tend to spread vertically and so overlap each other as one moves horizontally away from the sloping bottom. As a result, their penetration distance might be that required for the plumes to fully overlap. This distance and its slope-normal equivalent D can be estimated using the similarity solution of Koh (1966) (5.6), though it is unfortunately difficult to verify since D exceeds both the depth of our numerical domain and the depth of the ocean. Moreover, for small slopes the predicted D is proportional to the fourth power of the mean slope α_0 and the third power of the corrugation wavelength λ, so application to an ocean bottom with non-periodic corrugations and an uncertain mean slope will necessarily involve significant uncertainty. Nevertheless, (5.6) gives a physically relevant slope-normal length scale that deserves further consideration, and suggests the effect of the boundary layer might be felt over the full depth of the ocean.

Modelling results with a corrugated bottom also reveal two types of behaviour qualitatively different from that predicted by the analytical solution of Phillips/Wunsch for a constant slope. The constant-slope solution gives a reasonable approximation of the boundary-layer behaviour for small-amplitude corrugations (figure 4a), but as the corrugations get larger, we observe first spilling overflows (figure 4b), then reversing boundary-layer flows (figure 4c). These behaviours occur in distinct ranges of the dimensionless parameters λ/A and $\Delta h/A$ (figure 11). The boundary between these boundary-layer behaviours is predicted by the estimated bottom stress at the sill of the corrugation. If it is positive, we expect the point of boundary-layer separation to be downstream of the sill, giving an overflow. If it is negative, we expect the separation point to be upstream of the sill, giving a reversing boundary layer. The bottom stress can be estimated from the topography only (6.5).

These results are of potential oceanographic interest because observations of abyssal canyons show characteristics in common with these types of diffusive boundary layers, in particular bottom-intensified upslope flows, strong turbulence and layers of reduced stratification along the topography. The basic dynamics of the Phillips/Wunsch boundary layer provide a mechanism for upslope flow and reduced stratification, while the overflows observed in our numerical models might contribute to the strong turbulence. However, there are a number of complications to directly applying our results to the ocean. One key issue is the boundary-layer thickness. Using the parameter values from Thurnherr *et al.* (2005), the boundary-layer thickness δ given in (2.2) is about 60–80 m. At the same time, ocean observations show a layer of reduced stratification 300–600 m thick (see for example Thurnherr *et al.* 2005 and St. Laurent & Thurnherr 2007). Given the parameter ranges for overflows and reversing boundary layers summarized in figure 11 and the scale of mid-ocean ridge topography, the thinner estimate generally predicts a reversing boundary layer, while the thicker estimate layer is likely to create an overflow. St. Laurent & Thurnherr (2007) hypothesize that the thickness of the layer of reduced stratification is set by the height of the sills ($\delta \sim A$), not the internal dynamics of the boundary layer. This is consistent with our results, especially with the way that the boundary layer forces exchanges with the ambient fluids (for example see the secondary circulations in the troughs in figure 4c), but not a phenomenon we observed directly.

Our results therefore suggest that overflows at sills may be common in the deep ocean, but do not demonstrate it conclusively. Unfortunately, no currently available ocean data is high resolution enough on observe them, though we see suggestions of overflows in Thurnherr & Speer (2003), Thurnherr *et al.* (2005) and St. Laurent &

Thurnherr (2007). Numerous authors have discussed the dramatic increase in turbulent dissipation found near deep overflows (see for example Polzin *et al.* 1996 and Bryden & Nurser 2003). Though the overflows we modelled are much less energetic than observed deep overflows, even a small increase in turbulence may be significant, as there are $O(10^4)$ sills in ridge-flank canyons in the deep ocean (Thurnherr *et al.* 2005). This would produce a different distribution of deep ocean mixing in both space and time than the more extensively studied internal wave mechanisms, which could affect ocean circulation on the scale of the ocean basin.

Much work remains to be done if we are to understand the oceanographic implications of diffusive boundary layers like those studied here. This study covered only the most highly idealized version of the relationship between continuously varying bottom topography and diffusive boundary layers. In order to constrain the importance of these results for the deep ocean, future work will have to address the effect of rotation, three-dimensional topography, and the interaction among internal waves, turbulence and the boundary layer. Future work will also need to determine more conclusively what is setting the boundary-layer thickness in the ocean and how that affects boundary-layer flow. In addition, the authors note that the findings presented here are suitable for testing in a laboratory.

Acknowledgements

REFERENCES

BRYDEN, H. L. & NURSER, A. J. G. 2003 Effects of strait mixing on ocean stratification. *J. Phys. Oceanogr.* **33**, 1870–1872.

GARRETT, C. 1991 Marginal mixing theories. *Atmos.-Ocean* **29** (2), 313–339.

HUANG, R. X. & JIN, X. 2002 Deep circulation in the South Atlantic induced by bottom-intensified mixing over the midocean ridge. *J. Phys. Oceanogr.* **32**, 1150–1164.

KOH, R. C. Y. 1966 Viscous stratified flow toward a sink. *J. Fluid Mech.* **24** (3), 555–575.

ST. LAURENT, L. C. & THURNHERR, A. M. 2007 Intense mixing of lower thermocline water on the crest of the Mid-Atlantic Ridge. *Nature* **448**, 680–683.

MACCREADY, P. & RHINES, P. B. 1991 Buoyant inhibition of Ekman transport on a slope and its effect on stratified spin-up. *J. Fluid Mech.* **223**, 631–661.

MUNK, W. H. 1966 Abyssal recipes. *Deep-Sea Res.* **13**, 707–730.

PAGE, M. A. & JOHNSON, E. R. 2009 Steady nonlinear diffusion-driven flow. *J. Fluid Mech.* **629**, 299–309.

PEACOCK, T., STOCKER, R. & ARISTOFF, J. M. 2004 An experimental investigation of the angular dependence of diffusion-driven flow. *Phys. Fluids* **16** (9), 3503–3505.

PHILLIPS, O. M. 1970 On flows induced by diffusion in a stably stratified fluid. *Deep-Sea Res.* **17**, 435–443.

PHILLIPS, O. M., SHYU, J.-H. & SALMUN, H. 1986 An experiment on boundary mixing: mean circulation and transport rates. *J. Fluid Mech.* **173**, 473–499.

POLZIN, K. L., SPEER, K. G., TOOLE, J. M. & SCHMITT, R. W. 1996 Intense mixing of Antarctic bottom water in the equatorial Atlantic ocean. *Nature* **380**, 54–57.

SALMUN, H. & PHILLIPS, O. M. 1992 An experiment on boundary mixing. Part 2: the slope dependence at small angles. *J. Fluid Mech.* **240**, 355–377.

SHCHEPETKIN, A. F. & MCWILLIAMS, J. C. 2005 The Regional Ocean Modeling System (ROMS): a split-explicit, free-surface, topography-following-coordinate oceanic model. *Ocean Model.* **9**, 347–404.

THORPE, S. A. 1987 Current and temperature variability on the continental slope. *Phil. Trans. R. Soc. Lond.* A **323**, 471–517.

THURNHERR, A. M., ST. LAURENT, L. C., SPEER, K. G., TOOLE, J. M. & LEDWELL, J. R. 2005 Mixing associated with sills in a canyon on the midocean ridge flank. *J. Phys. Oceanogr.* **35**, 1370–1381.

THURNHERR, A. M. & SPEER, K. G. 2003 Boundary mixing and topographic blocking on the Mid-Atlantic Ridge in the South Atlantic. *J. Phys. Oceanogr.* **33**, 848–862.

UMLAUF, L. & BURCHARD, H. 2011 Diapycnal transport and mixing efficiency in stratified boundary layers near sloping topography. *J. Phys. Oceanogr.* **41**, 329–345.

WELDON, M., PEACOCK, T., JACOBS, G. B., HELU, M. & HALLER, G. 2008 Experimental and numerical investigation of the kinematic theory of unsteady separation. *J. Fluid Mech.* **611**, 1–11.

WUNSCH, C. 1970 On oceanic boundary mixing. *Deep-Sea Res.* **17**, 293–301.